Applied Catalysis B: Environmental 258 (2019) 117947

Contents lists available at ScienceDirect

Applied Catalysis B: Environmental

journal homepage: www.elsevier.com/locate/apcatb

ZIF derived PtNiCo/NC cathode catalyst for proton exchange membrane fuel cell

Saadia Hanif[a,b,1], Xuan Shi[b,1], Naseem Iqbal[a,*], Tayyaba Noor[c], Rehan Anwar[a,b], A.M. Kannan[b,**]

[a] USPCAS-E, National University of Sciences and Technology, Islamabad 44000, Pakistan
[b] Fuel Cell Laboratory, The Polytechnic School, Ira A. Fulton Schools of Engineering, Arizona State University, Mesa, AZ 85212, USA
[c] SCME, National University of Sciences and Technology, Islamabad 44000, Pakistan

ARTICLE INFO

Keywords:
ZIF-67
PEMFC
ORR
Electrocatalyst
PtNiCo/NC

ABSTRACT

High performance cathode catalysts with minimum platinum amount for the electrocatalyzed oxygen reduction reaction (ORR) in PEMFCs remain as a significant challenge for commercial application. Zeolitic Imidazolate Framework (ZIF) based catalyst can provide void 3D framework of N-doped nano-porous carbon for promising ORR activity. Here we report a bimetallic pyrolyzed NiCo-ZIF supported fine Pt/Pt alloy electrocatalyst for ORR. After pyrolysis, nano-porous carbon is obtained with well dispersed Pt/Pt alloy nanoparticles (~ 3 nm). This catalyst shows superior performance and stability in acidic medium against the commercial catalyst comprising of Pt/C. In a single cell PEMFC, high peak power density value of 1067 mW. cm^{-2} is attained at 70 °C by using low platinum amount of 0.12 mg cm^{-2} on cathode. The enhanced activity and durability is credited to the synergistic impact of N-doped nano-porous carbon originated from NiCo-ZIF and the defect rich carbon support to anchor Pt/Pt alloy nanoparticles.

1. Introduction

Ever increasing worldwide energy demand has encouraged researchers to explore various non-conventional sources of energy generation. Fuels cells have the benefit of furnishing energy with high efficiency and negligible environmental pollution. In prevailing technologies for fuel cells, the PEM based fuel cells have an edge of generating superior power density along with quicker start-up time, and moderate operating condition of temperature. In addition, the fuel cells have been efficiently established with an aim to power the imminent electrical transportation, handy electronic devices and heavy duty applications [1,2]. To promote the redox reactions on both the anodes and cathodes in a PEMFC, Pt metal supported on carbon is being employed. However, due to slow reaction kinetics, ~ 30 g of Pt is employed to power a Toyota Mirai [3]. The main hindrance in widespread commercial applications of PEM fuel cell remains the stability, cathode activity and cost factor [4,5]. A cathode catalyst without precious Pt is preferred but the fuel cell activity and catalyst durability in acidic medium is a challenge [6–8]. Thus, to develop a stable catalyst towards oxygen reduction reaction (ORR) that can eliminate or lessen the platinum metal loading without compromising the proficiency of the PEM fuel cell is at the heart of research today [9–11].

In recent years, the nano-porous versatile class of compounds such as metal-organic frameworks (MOFs) are unfolded as encouraging materials in different emerging areas like heterogeneous catalysis, gas adsorption, and drug delivery applications [12–14]. ZIF is one of MOFs with imidazole as an organic linker with metal; it has rich carbon, nitrogen and the transition metal. The bonds formed between nitrogen atoms and metal nanoparticles served as catalytic sites during ORR [15]. These ZIF derived nano-porous carbon composites demonstrate better ORR activity in alkaline medium but have poor long-term stability in acidic medium [16]. Decomposed ZIFs have been reported to support Pt nanoparticle for ORR catalyst in acidic fuel cell. Hence the Pt catalyst loading can be reduced, as ZIF not only acts as a conducting network but also has the intrinsic ability to catalyze the reaction [17]. Pt consumption can be improved by moderating the particle size of Pt/Pt alloy. Single atom Pt catalyst is reported to enhance the PEMFC performance [18]. The single atom of Pt is weak during the long-time operation due to the Ostwald ripening, proper anchor should be addressed in order to fix the single Pt atoms [19]. The defects e.g. O—C, O═C [20], N—C [21], could effectively increase the stability of Pt nanoparticles. PtNi alloy has a significant performance for ORR and actively

* Corresponding author.
** Corresponding author.
E-mail addresses: naseem@uspcase.nust.edu.pk (N. Iqbal), amk@asu.edu (A.M. Kannan).
[1] Saadia Hanif and Xuan Shi contributed equally.

https://doi.org/10.1016/j.apcatb.2019.117947
Received 19 March 2019; Received in revised form 8 July 2019; Accepted 9 July 2019
Available online 13 July 2019
0926-3373/

pursued as catalyst for fuel cell cathode [22–25]. However, these catalysts have stability issues, complicated synthesis techniques and require large amount of Pt loading [26]. Recently Chong et al. have studied the Pt-Co catalyst derived from imidazolate frameworks with ultralow Pt loading and demonstrated excellent performance in PEMFC. The reported work shows the prospect of Pt based cathode catalyst for ORR in PEMFC [27].

Herein, we report a significantly higher PEMFC activity with the cathode of PtNiCo/NC containing Pt/Pt alloy as well as Pt single atoms derived from bimetallic NiCo-ZIF.

2. Experimental

2.1. Synthesis of Co-ZIF

In a representative procedure, solutions of 1.97 g of linker 2-methylimidazole in 20 ml of MeOH and 1.746 g of Cobalt(II) nitrate hexahydrate in 60 ml of MeOH were mixed for 30 s with stirring. Resulting mixture was held for 24 h at ambient temperature. The purple color product was centrifuged, washed in MeOH multiple times and dried in air at 80 ℃ [28]. The Co-ZIF is used mainly for performance comparison with NiCo-ZIF.

2.2. Synthesis of NiCo-ZIF

Similar to previously described procedure, solution of 1.97 g of 2-methylimidazole in 20 ml of MeOH, 873 mg of Cobalt(II) nitrate hexahydrate and 873 mg of Nickel(II) nitrate hexahydrate in 60 ml of MeOH was continuously stirred for 24 h at ambient temperature. The resultant product crystal was separated by centrifugation, and followed by multiple times washing in MeOH and dried in air at 80 ℃.

2.3. Synthesis of PtNiCo/NC

The NiCo-ZIF particles were mixed in $H_2PtCl_6.6H_2O$ solution (5 wt. %) and dried at 80 ℃ for 3 h. The resultant powder was heated to 350 ℃ in a ceramic boat in a tube furnace for 1.5 h. The temperature is further increased to 700 ℃ at 2 ℃ per min and held for 3.5 h under Ar/H_2 flow (90/10). The product was stirred for 6 h in 0.5 M H_2SO_4. The product was centrifuged, repetitively washing with deionized H_2O and subsequently vacuum dried at 80 ˚C.

2.4. Catalyst characterization and elemental analysis

The powder XRD measurements were carried out in a Siemens D5000 X-ray Powder Diffractometer having Co anode (Co Kα 1.79 Å). The diffraction data were collected from 5 to 29 and 20 to 70 2θ degrees for ZIF samples and pyrolyzed ZIF samples, respectively, with 0.02 2θ degrees per second. The reason why to choose Co instead of Cu target is that the Co containing samples has greatest fluorescence under Cu Kα, this will lead to low signal to noise ratio. It could be solved by applying longer wavelength Co Kα X-ray. The surface morphology of synthesized catalyst samples was analyzed by using Field emission scanning electron microscopy (FESEM) (HITACHI S-4700 with 5–10 keV). Transmission electron microscopy (TEM) measurements were carried out by CM200-FEG (Philips) at 200 keV. High Angle Annular Dark Field (HAADF) analysis along with energy dispersive spectroscopy (EDS) was recorded by employing a scanning transmission electron microscopy STEM (JEM-ARM200 F) at power of 200 keV. VG 220i-XL was used to measure X-ray Photoelectron Spectroscopy. Inductively coupled plasma mass spectrometry (ICP-MS) analysis was carried out by taking 5 mg of PtNiCo/NC ashes (oxidized at 800℃ for 2 h) with 3 ml and 1 ml trace metal grade of HCl and HNO_3, respectively. The mixture was agitated and then kept at 80 ℃ overnight for metal digestion. After filtering out the undigested ashes, the sample was diluted to the detection limit with DI water and measured on Thermo Scientific's iCAP Q quadrupole ICP-MS using an Elegra Argon humidifier.

2.5. Electrochemical evaluation on rotating disk electrode

The ORR performance was evaluated with PtNiCo/N-doped carbon (NC) and NiCo/NC materials on rotating disk electrode (RDE). For comparison, commercial Pt/C (46.1 wt% from Tanaka Kikinzoku Kogyo, TEC10E50E) was also employed. 5 mm working glassy carbon (GC) electrode (Pine Research AFE5T050GC) was prepared by specific amount of catalyst inks. The catalyst ink was made by addition of 5 mg carbon catalysts in 2.4 ml of IPA, 7.6 ml of DI H_2O, and 0.1 ml of a 5 wt. % Nafion dispersion (Ion power LQ-1105 - 1100 EW, 5 wt. %). Approximately 25 $\mu g_{Pt}\,cm^{-2}$ is applied when the sample contains Pt then dried in hot air with at 700 rpm to obtain a uniform thin film. For non-Pt catalysts, a 700-μg cm^{-2} were applied. The electrochemical measurements were evaluated in 0.1 M $HClO_4$ solution with saturation of N_2 and O_2. In three electrode setup, Pt wire was used as counter electrode (CC) along with reference saturated calomel electrode (SCE). RDE measurements for ORR were conducted at 20 mVs^{-1}. ORR activity in terms of polarization curves were acquired at 400, 800, 1200 and 1600 rpm. Stability testing of PtNiCo/NC and commercial employed Pt/C catalyst was measured in 0.1 M $HClO_4$ solution at ambient temperature and oxygen-saturated environment. Voltage cycling from 0.5 to 1.1 V was conducted for 5000 cycles against reversible hydrogen electrode (RHE) with scan rate of 200 mVs^{-1}.

2.6. Electrode fabrication and fuel cell performance

2.6.1. Catalyst coated membranes

The cathode and anode catalyst layers were directly coated on the Nafion-212 membrane with micro-spray method. Catalyst was dispersed in 5 wt. % Nafion dispersion and IPA to prepare ink. The platinum loading on anode (commercial Pt/C) and cathode is 0.12 and 0.12 $mg_{Pt}\,cm^{-2}$, respectively. Same amount of Pt loading was applied for reference MEA on cathode with commercial Pt/C. In case of non-Pt cathode, the ionomer catalyst ratio was ˜1:2 and the catalyst amount was ˜ 3.5 mg. cm^{-2}.

2.6.2. Gas diffusion layer

For GDL fabrication, graphitized non-woven carbon paper (GD07508 G) was employed as substrate from Hollingsworth & Vose Company. Carbon slurry was prepared by using Nano-chain Pureblack carbon (grade 205-110 Superior Graphite Company), Teflon dispersion (DISP 30, Fuel cell earth Company), vapor grown carbon fiber (VGCF Showa Denka) along with sodium dodecyl sulfate (SDS) (Fisher Scientific). Solution of 120 mg sodium dodecyl sulfate (SDS) and 0.5 g carbon powder (75 wt% Pure black carbon powder and 25 wt% VGCF) in 6.5 ml of deionized H_2O was sonicated for 30 min and then stirred at 60 rpm for 60 min. Under gentle stirring, 30% Teflon dispersion (Fuel Cell Earth) dispersion was mixed. For carbon slurry coating on non-woven carbon paper substrate (10 cm x 10 cm) Easy coater equipment (EC26, Coatema) was used at speed of 3 m min^{-1}. After drying overnight at ambient air, sintered in air at 350 ˚C for 30 min and then immersed in deionized H_2O for 30 min to remove SDS. The calculated amount of carbon loading on the GDL was ˜3 mg cm^{-2} [29].

2.6.3. Single fuel cell performance

Single fuel cell was made by stacking all the components with an active area of 5 cm^2. Fuel cell performance was assessed on G40 fuel cell test station, (Hydrogenics, Canada) at 75 ˚C with fully humidified conditions. A gas flow of 200 (anode) and 300 (cathode) SCCM was applied. After activation of MEA at 0.5 V, voltage was stepwise decreased to 0.2 V with 20 mV per minute and increased back up to 0.5 V with similar step size. The stability test was similar to the activation process, except after reaching 0.2 V, the polarization curve was

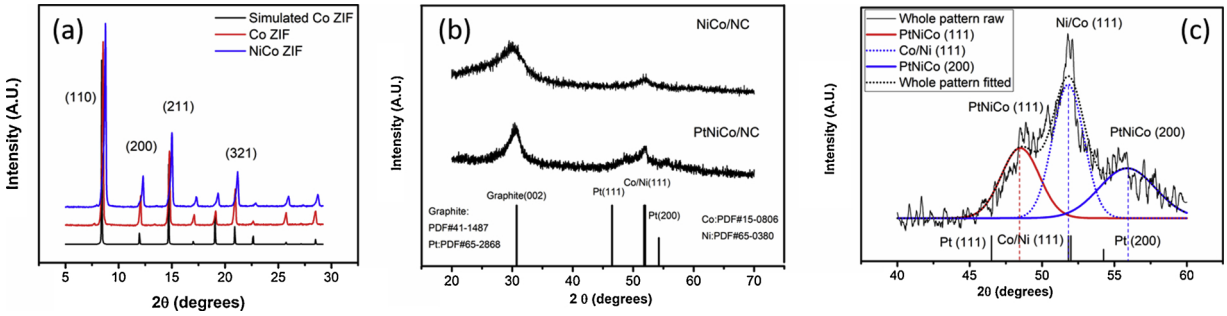

Fig. 1. XRD of (a) Co ZIF (red) and NiCo ZIF (blue) along with simulated pattern for Co ZIF (black), (b) NiCo/NC and PtNiCo/NC, and (c) high resolution XRD looping scan for Pt, Ni, Co (111) regions. (For interpretation of the references to colour in this figure legend, the reader is referred to the web version of this article.)

collected. The program was cycled until it reached 100 h and the peak power densities were selected for plotting.

3. Results and discussion

Fig. 1a displays the simulated Co-ZIF, as prepared Co-ZIF and NiCo-ZIF. The simulated diffraction pattern is matching the recorded Co-ZIF pattern, indicating the successful synthesis of Co-ZIF. When adding Ni precursor during the synthesis, the diffraction pattern remains same but slightly shifted to the higher 2θ angle. This shifting explains that Ni replaced some of the Co ion in the imidazole framework and gave a smaller d spacing due to the shifting to the higher 2θ angle. For the pure Ni and Co metals (111) plane, the Ni has higher diffraction angle compared to the Co at 51.830 and 51.998, respectively. Fig. 1b shows the XRD of NiCo/NC and PtNiCo/NC. Both samples have clear graphite (002) diffraction peaks at ˜30.72 2θ degrees while the samples with Pt precursor have sharper/narrower diffraction peaks indicated the carbon has better crystallinity compared to the sample NiCo/NC. The NiCo/NC both have broad peaks at ˜ 52 2θ degrees due to the Co (111) and Ni (111) diffraction at 51.830 (PDF#15-0806) and 51.988 (PDF#65-0380) 2θ degrees. The alloy has been confirmed for PtNiCo/NC by the broad diffraction peaks are shifting away from the Pt (111) at 46.510 (PDF#65-2868) 2θ degrees. Fig. 1c is showing the deconvoluted diffraction pattern of PtNiCo/NC has three peaks, PtNiCo (111), Ni/Co (111) and PtNiCo (200) at 48.42, 51.81 and 55.92, respectively. The $Pt_{2.45}$(Ni/Co) is estimated to be the alloy formula. In PtNiCo/NC sample, there are some unalloyed (Ni/Co) particles due to the Ni/Co (111) diffraction. The full width half maximum (FWHM) from the deconvoluted peaks provides more information regarding crystallite size. The size of PtNiCo and Ni/Co are estimated to be 3.1 and 3.5 nm. The diffraction peaks position, lattice spacing, Pt:(Ni/Co) ratio and FWHM analysis of PtNiCo/NC is summarized in Table 1.

The Fig. 2a, b show SEM images of Co-ZIF and NiCo-ZIF. The size of NiCo-ZIF particles (˜0.5 µm) is smaller than Co-ZIF particles (˜2 µm). The Co-ZIF shows hexagonal based polyhedron while the NiCo-ZIF shows a cubic polyhedron. The difference after adding Ni precursor not only modified the shape of ZIF but also reduced the particle size during the solvothermal synthesis. After heat treatment of NiCo-ZIF and acid washing, the hollow structures is covered with interconnected carbon nanotubes (CNTs) showing in Fig. 2c. Same observations are reported in reference [28,30,31]. Under Ar/H_2 environment, the Co/Ni ion is reduced by the H_2 gas at 700 °C, the Co/Ni metal will act as seed widely spread out in the carbon rich ZIF. In the meantime, the ZIF starts to decompose, evaporate the unstable organic groups, left mostly carbon in the sample. The heated carbon atoms start to move around under temperature, they are favorable to dissolve into heated seeds. When the seeds get saturated with carbon atoms, the bottom-up growing starts to begin [32]. The XRD showed broader peak for graphite (002) plane compared to the sample with Pt, this can conclude the CNTs only limited on the surface, the majority carbon is present as amorphous carbon inside the decomposed ZIF. Interestingly, no CNTs can be seen on the Pt loaded ZIF particle surface at high temperature. The surface of the particles gets rougher and forms nano-porous carbon and the size is also shrunk under pyrolysis (Fig. 2d). The possible reason for no CNTs is because of occurrence of Pt precursor, the reduced Pt atoms tends forming alloy with Ni/Co. The XRD showed more Pt compare to the Ni/Co, so the Ni/Co was buried into Pt then inhibited the formation of CNTs.

The HAADF image is showing in Fig. 3a, the blueness is due to the thickness of the NiCo-ZIF. In the selected area in the green box, the EDS signal was collected. The element mapping is showing in the Fig. 3b. C, N, Co and Ni are well dispersed into the ZIF material and the Ni mapping is relatively sparse in the structure. The well dispersed metal/metal alloy supported by the amorphous carbon with particle size ˜2–3 nm can be viewed in the Fig. 3c. The study shows that the Pt particle at around 2.2 nm is supposed to have the highest PEMFC activity [33]. The lattice spacing can be seen in Fig. 3d at 0.21 nm attribute to Pt/Ni or Co alloy (111) plane. From the Table 1, the d-spacing of Pt and Ni/Co (111) plane are 0.227 and 0.204/0.205 nm, respectively. The contracting Pt (111) plane is also an indication for the formation of the alloy. Also, single atoms can be seen nearby the big island of atoms. The single atoms can be highly efficient for catalyzing reactions, due to (1) surface effects, the percentages of unsaturated bonds increases with particle downsizing and reach the max in single atom; (2) the energy level of single atom will increase due to quantum confinement and widen the Kubo gap and (3) the metal support interactions is stronger [34]. However, under harsh environment in PEMFC, the single atom will need strong defects to anchor in order to conquer the Ostwald ripening [19].

The Fig. 4 shows the XPS data for PtNiCo/NC. The survey scan is displayed in Fig. 4a, from all the XPS peaks, there are 94.42, 0.72, 2.57, 2.11 and 0.18% of C, N, O, Pt and Co, respectively. The XPS didn't

Table 1
The diffraction peaks position, lattice spacing, Pt:(Ni/Co) ratio and FWHM analysis of Pt, Co, Ni, PtCo and PtNiCo.

	Pt (111) PDF#65-2868	Co (111)/Ni (111) PDF#15-0806/ PDF#65-0380	PtNiCo (111)	Ni/Co (111)
Diffraction Angle (2θ degrees)	46.51	51.83/51.98	48.42	51.81
Lattice spacing (A)	2.27	2.05/2.04	2.18	2.05
Pt : (Ni/Co) Alloy ratio	–	–	2.45	–
Scherrer FWHM estimation (nm)	–	–	3.1	3.5

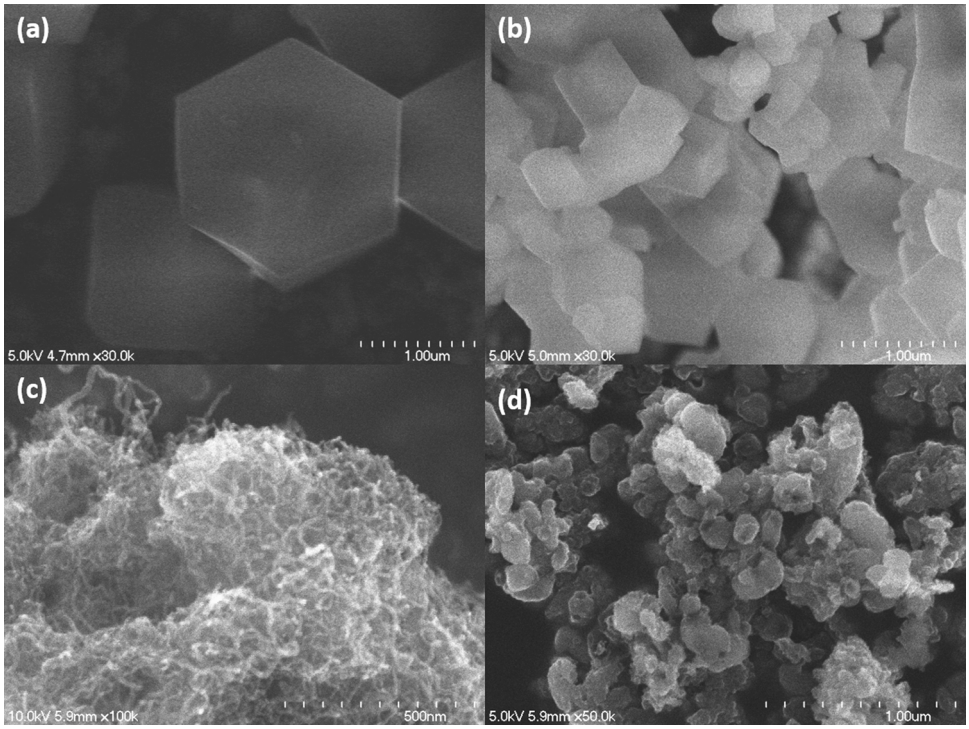

Fig. 2. Scanning Electron Micrographs of (a) Co-ZIF, (b) NiCo-ZIF, (c) NiCo/NC, (d) PtNiCo/NC.

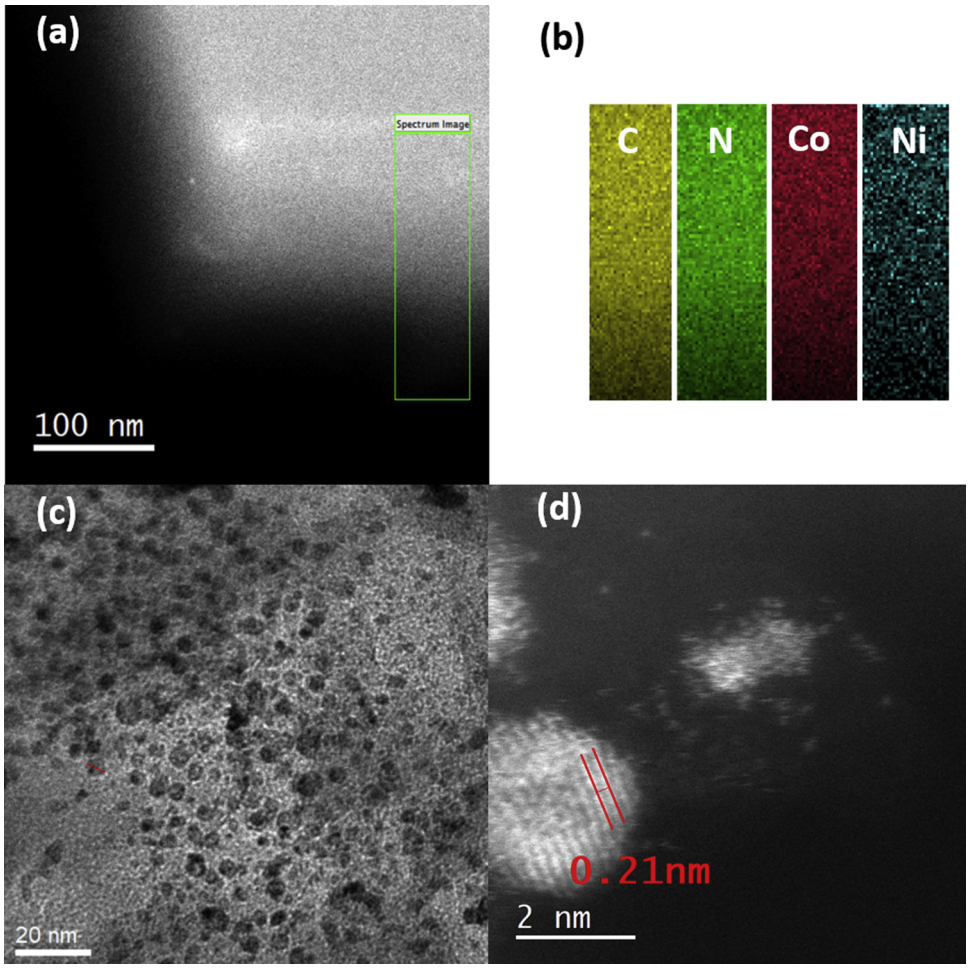

Fig. 3. (a) The HAADF image of NiCo-ZIF, (b) EDS mapping of selected area from (a), TEM (c), (d) STEM image of PtNiCo at different magnification.

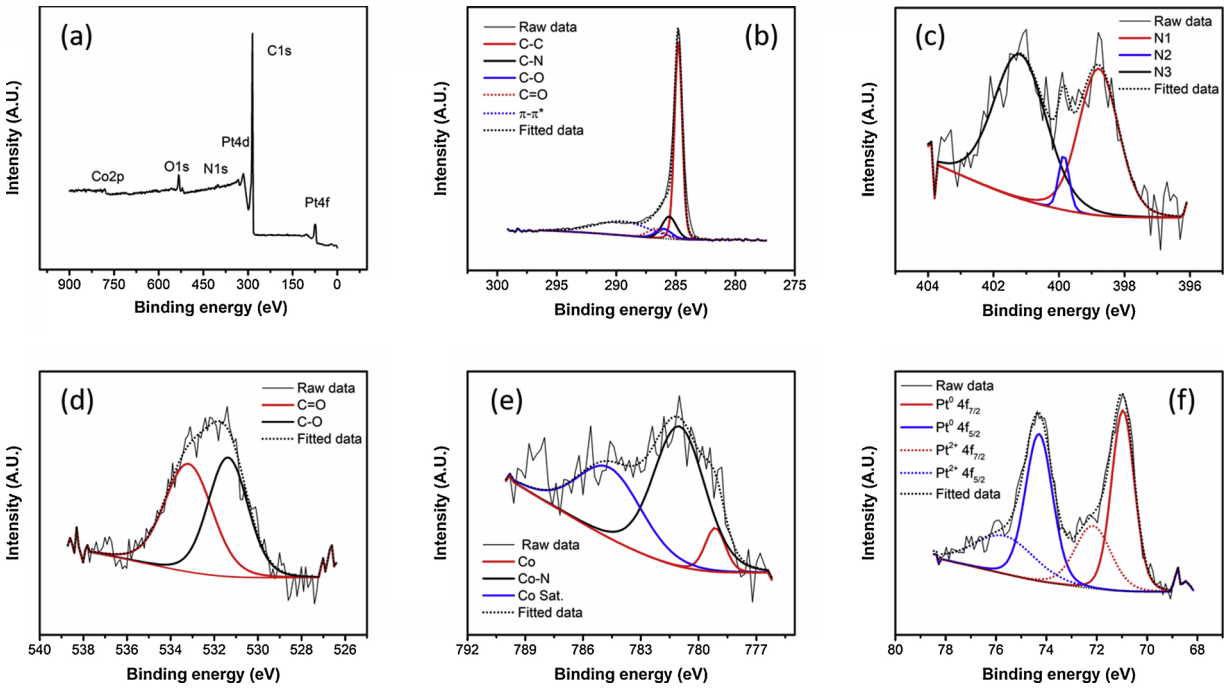

Fig. 4. (a) The wide scan of XPS data and the deconvoluted high resolution XPS scan of (b)C1s, (c)N1s, (d) O1s, (e) Co2p and (f) Pt4f.

resolve Ni signal due to less % of Ni than the detecting limit. But from the ICP-MS analysis, the Pt, Ni and Co are 68.0, 0.6 and 31.4 at. %, respectively. For the detailed bonding information, the C1s high resolution scan is showing in Fig. 4b. Total five C bonding, C—C (284.8 eV), C–N (285.4 eV), C–O (286 eV), C═O (286.6 eV) and p-p* (291.3 eV) are resolved in PtNiCo/NC [35,36]. The N doping was also confirmed in Fig. 4c, N1, N2 and N3 stands for the pyridinic N (398.7 ± 0.3 eV), imine/amide/amine (399.8 ± 0.2 eV) and pyrrolic N (400.3 ± 0.2 eV) [37]. The N1, N2 and N3 has 43.14, 4.31 and 52.55 at% from XPS surface quantification analysis. The N1 and N3 are believed to have positive effect towards ORR [38,39] also the type of N will determine the oxidation state of transition metal and platinum group metal [40]. O═C and O—C bonding are deconvoluted in O1s XPS in Fig. 4d, the small amount of oxygen content is due to oxidation during the pyrolysis. The defects rich carbon support is acting as anchor for Pt/Pt alloy particles even single Pt atoms [20,21]. Fig. 4e shows the Co 2p XPS, three peaks are resolved, Co^0(779.1 eV), Co^{2+} (781.6 eV) and Co $2p_{3/2}$ (785.2 eV) shake up satellite peak. The Co^0 can be attributed to the Co and Pt alloy, the ionic Co belongs to Co-N coupling [35]. Co-*N*-C is also believed to act as an active site to catalyze the ORR in acidic media [15]. High resolution Pt 4f XPS is showing in Fig. 4f, four distinct peaks are resolved of Pt^0 $4f_{7/2}$ (71.0 eV), Pt^{2+} $4f_{7/2}$ (72.3 eV), Pt^0 $4f_{5/2}$ (74.4 eV), Pt^{2+} $4f_{5/2}$ (75.6 eV) [41]. The ratio of Pt^0 to Pt^{2+} is around 4.17:1. From the XPS data, the Pt composition for

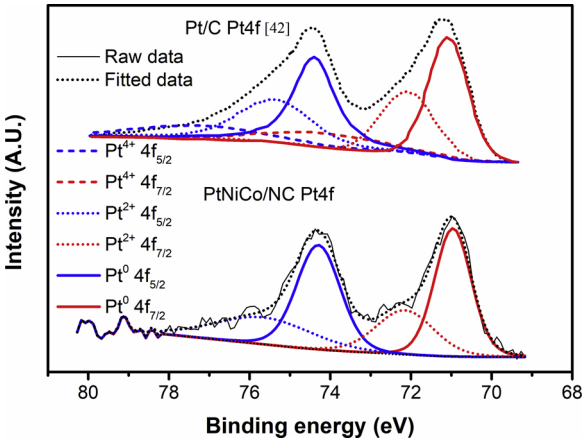

Fig. 5. Comparison of Pt4f spectra of PtNiCo/NC and Pt/C from XPS.

both the Pt/C (commercial) and PtNiCo/NC were estimated by peak quantification and is shown in Table 2. As given in Table 2, the Pt^0 is 51 and 64 atomic % for commercial Pt/C and PtNiCo/NC, respectively [42]. Even though, the Pt/C (commercial) showed the occurrence of Pt^{2+} and Pt^{4+}, the PtNiCo/NC catalyst only showed Pt^{2+} signals. The

Table 2
The atomic percentage for deconvoluted components from XPS data.

	Total at. %	at. % for each component				
C	94.42	52.2 (C-C)	11.7 (C-N)	5.35 (C-O)	5.2 (C = O)	26.8 (π−π*)
N	0.72	43.14 (N1)	4.31 (N2)	52.55 (N3)		
O	2.57	50.00 (C = O)	50.00 (C-O)			
Ni	–	–	–	–	–	
Co	0.18	10.40 (Co^0)	89.60 (Co^{2+})			
Pt (PtNiCo/NC)	2.11	32.62 (Pt^0 $4f_{7/2}$)	17.76 (Pt^{2+} $4f_{7/2}$)	31.65 (Pt^0 $4f_{5/2}$)	17.97 (Pt^{2+} $4f_{5/2}$)	

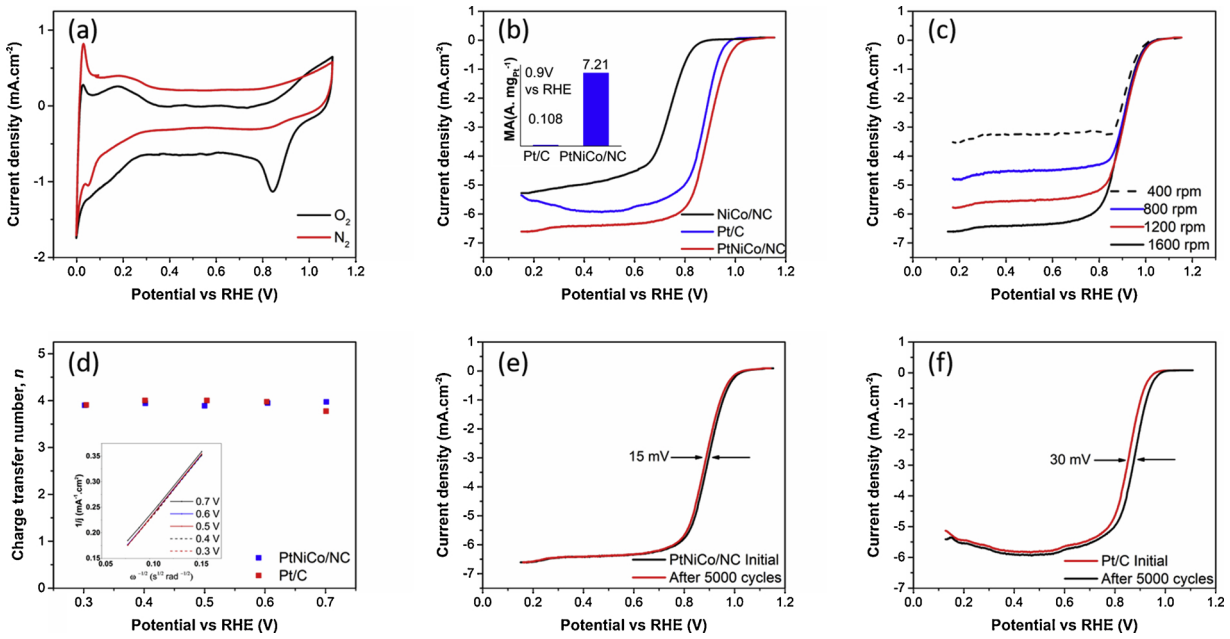

Fig. 6. Electrochemical oxygen reduction on PtNiCo/NC (a) CV profiles (red and black curves indicate CV curves recorded in N_2- and O_2-saturated 0.1 M $HClO_4$ solution, respectively). (b) LSV curves of different samples at O_2-saturated 0.1 M $HClO_4$ solution at 1600 rpm. Insert, The comparison of MAs at 0.85 V versus RHE (c) LSV curves at different rotation rates (rpm) for PtNiCo/NC (d) Charge transfer number (n). Insert, K–L plots, ω is the angular rotation speed. (e) Durability Test: ORR polarization curves (1600 rpm) of PtNiCo/NC before and after 5000 cycles. (f) Durability Test: ORR polarization curves (1600 rpm) of Pt/C before and after 5000 cycles. (For interpretation of the references to colour in this figure legend, the reader is referred to the web version of this article.)

Table 3
Comparison of different as prepared samples and commercial Pt/C used as electrocatalysts for ORR in acidic medium.

Electrocatalysts	Onset Potential[a] (V vs RHE)	Half wave Potential (V vs. RHE)	Loading	Limiting current density at 0.1 V vs. RHE mA. cm^{-2}
PtC	0.98	0.87	25 $\mu g_{Pt}/cm^2$	5.50
NiCo/NC	0.86	0.76	0.7 mg/cm^2	5.55
PtNiCo/NC	1.03	0.91	25 $\mu g_{Pt}/cm^2$	6.51

[a] vs. RHE, read at current density of 0.05 mA·cm^{-2} from Fig. 6b.

introduction of Ni and Co reduces the oxophilicity of Pt leading to enhanced fuel cell performance [43,44]. The Table 2 also summarized the rest atomic percentage of each element and the ratio of deconvoluted components. Overall, the XPS demonstrates the Pt and transition metal are strongly interacting with each other and the N, O functional groups on carbon support (Fig. 5).

Firstly, the electrocatalytic efficiency of the PtNiCo/NC is evaluated by cyclic voltammetry (CV). When the $HClO_4$ solution is saturated with nitrogen, no redox peak was observed, as shown in Fig. 6a. After saturation with O_2 gas, a distinct cathodic peak is detected due to oxygen reduction. Linear sweep voltammetry (LSV) was conducted using rotating disk electrode (RDE) set-up at various rotation rates. The ORR performance of NiCo/NC is also evaluated by LSV. NiCo/NC shows reasonable performance at 1600 rpm as revealed by the value of onset potential at 0.86 V vs. RHE and peak current density of 5.55 mA. cm^{-2}. When Pt is added to these samples, the ORR activity is considerably improved. The PtNiCo/NC showed the best performance for ORR as indicated by the onset potential value at 1600 rpm. Comparison of PtNiCo/NC with the commercially employed Pt/C catalyst for the ORR is presented in Fig. 6b. At 1600 rpm PtNiCo/NC shows onset potential value of 1.03 V due to 50 mV positive shift against Pt/C. Fig. 6b inset shows the mass activities are 7.21 and 0.108 A.mg_{pt}^{-1} at 0.9 V vs RHE for PtNiCo/NC and Pt/C, respectively. N-doped nano-carbon, Co/Ni catalytic sites, Pt/Pt alloy as along with single Pt atoms could be the mutually reinforcing factors for triggering exceptional ORR performance for PtNiCo/NC [24,18,45,46]. With the increase in rpm, values of current densities also increase for PtNiCo/NC (Fig. 6c). Koutecky-Levich (K–L) equation was utilized to calculate the kinetic parameters. The linear K–L plots indicate fast reaction kinetics regarding dissolved oxygen for the potential range 0.7-0.3 V and the reaction is controlled by diffusion [46,47]. The electron transfer numbers (n) at 0.7-0.3 V is calculated to be in range of ˜3.97-3.98 which is same as compare to commercial Pt/C. This indicates a complete 4e- ORR pathway conforming complete reduction of oxygen (Fig. 6d) [48]. Summary of the performance of all prepared samples and commercial Pt/C in RDE is summarized in Table 3. provides. The PtNiCo/NC electrocatalyst was further tested with CV to determine the durability of the catalyst in acid. After 5000 CV cycles from 0.5 to 1.1 V, PtNiCo/NC catalyst shows negligible loss in performance determined by the LSV curve. In terms of

Table 4
Comparison of different Pt based electrocatalysts for ORR in acidic media (ORR test conditions: 1600 RPM, 0.1 M $HClO_4$).

Electrocatalysts	Onset Potential V vs RHE	Halfwave Potential V vs RHE	Loading $\mu g_{Pt}/cm^2$	Limiting current density at 0.1 V vs. RHE mA.cm^{-2}	Scan rate mV/s	Reference
Pt_1-N/BP	0.94	0.76	24	4.8	5	[18]
Pt/Zr–C 3	0.90	–	40	5.7	10	[49]
$Pt_{0.61}Ni/C$	–	0.85	24	5.2	5	[23]
PtNi@Pt	0.95	–	12	6.0	10	[25]
PtNiCo/NC	1.05	0.91	25	6.5	20	This work

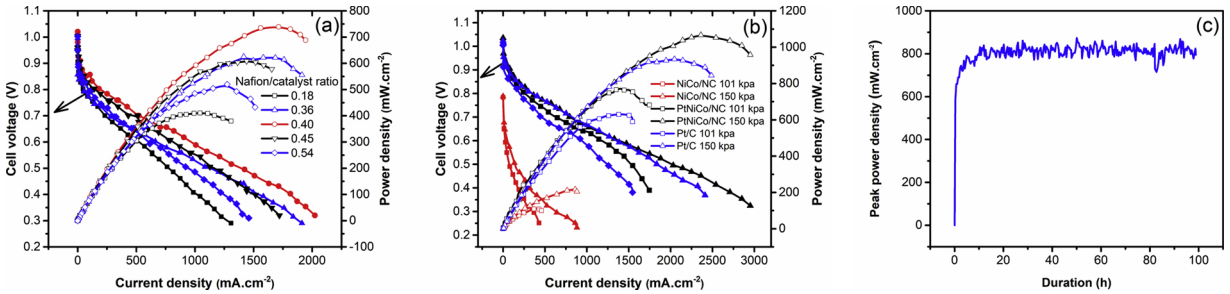

Fig. 7. The PEMFC performance of (a) Nafion/catalyst ratio optimization for PtNiCo/NC, (b) MEAs with NiCo/NC, PtNiCo/NC and Pt/C with/without back pressure, (c) the stability testing with PtNiCo/NC cathode at ambient pressure. (All the data were obtained at 70 °C, 100% relative humidity with H_2 and O_2 at 200 and 300 SCCM with Nafion212 membrane.).

halfwave potential, there is negative shift of 15 mV at 1600 rpm compared to 30 mV in case of Pt/C commercial catalyst (Fig. 6e–f). A comparison of Pt catalyst published by different group is displaying in Table 4.

To optimize catalyst utilization, the influence of Nafion concentration on the fuel cell performance (Fig. 7a) was evaluated. Various ratios of Nafion to PtNiCo/NC catalyst amount at 70 °C using H_2 and O_2 gases at 100% RH at ambient pressure was studied. As observed from Fig. 7a, the ratio of 0.4 exhibited the highest peak power density of 740 mW.cm^{-2} without any back pressure. Fuel cell activity is compared in Fig. 7b for PtNiCo/NC cathode catalyst based MEA (optimized Nafion to catalyst ratio of 0.4) with that of NiCo/NC and commercial Pt/C at 70 °C with H_2 and O_2 gases at 100% RH with (150 kpa) and without (101 kpa) back pressures. The cathode catalyst NiCo/NC without Pt exhibited a relatively lower peak power density of 211 mW.cm^{-2}. In addition, the MEA with NiCo/NC cathode catalyst also showed lower OCV (< 0.8 V) due to extremely high activation polarization associated with the ORR. As expected from the RDE results (Fig. 6b), the PtNiCo/NC exhibited the highest peak power density of 1070 mW.cm^{-2} at 150 kpa and the commercial Pt/C led to 930 mW.cm^{-2} at 150 kpa. Evidently, the mass activity value for the PtNiCo/NC cathode catalyst is higher (~9 W.mg$_{Pt}^{-1}$) against the Pt/C commercial catalyst (~7.8 W.mg$_{Pt}^{-1}$) due to the synergistic effect of the elements in the alloy. The PtNiCo/NC cathode catalyst based MEA evaluated for 100 h at 100% RH with H_2 and O_2 at atmospheric pressure showed excellent stability. The peak power density values did not exhibit any performance degradation, demonstrating well anchored platinum alloy particles on carbon support (Fig. 7c). The fluctuations are mainly due to the water management in the PEMFC single cell.

4. Conclusions

In the present study, highly efficient and durable PtNiCo/NC catalyst was prepared, derived from NiCo-ZIF towards ORR. XRD showed that with the introduction of the Pt precursor, higher carbon crystallinity is obtained, to provide a higher conducting carbon matrix. By changing Co^{2+} with Ni^{2+} composition in the zeolitic imidazolate frameworks, size of ZIF particles is reduced as depicted in SEM. The Pt/Pt alloy with the size 2–3 nm as well as single Pt atoms are anchored with defects rich carbon support as confirmed by STEM and XPS. For ORR, value of onset potential is 1.03 V and the value of limiting current density is 6.51 mA. cm^{-2}. The durability in acidic medium is better with respect to commercial catalyst Pt/C. PtNiCo/NC eelctrocatalyst in single cell activity showed peak power density of 1070 mW. cm^{-2} at 150 kpa, 70°C and 100% RH with H_2 and O_2 which is ~15% increase with same Pt loading at identical testing conditions. A 100 h stability test showed no degradation with PtNiCo/NC MEA. These results reinforce the superior performance of the alloy catalyst over the traditional Pt/C catalyst related to durability and activity for ORR.

Declaration of Competing Interest

None.

Acknowledgements

Financial support by United States Agency for International Development and U.S.-Pakistan Centers for Advanced Studies in Energy is highly acknowledged. Eyring Materials Center at Arizona State University is highly acknowledged for the use of facilities. We would also like to thank Pakistan Science Foundation for the support under Project No. PSF-NSF/Eng/C-NUST (04).

References

[1] M.K. Debe, Electrocatalyst approaches and challenges for automotive fuel cells, Nature 486 (2012) 43, https://doi.org/10.1038/nature11115.
[2] A. Rabis, P. Rodriguez, T.J. Schmidt, Electrocatalysis for Polymer Electrolyte Fuel Cells : Recent Achievements and Future Challenges, ACS Catal. (2012), https://doi.org/10.1021/cs3000864.
[3] M.S. Naomi Tajitsu, Toyota Plans to Expand Production, Shrink Cost of Hydrogen Fuel Cell Vehicles, (2018) https://www.reuters.com/article/us-toyota-hydrogen-idUSKBN1KG0Y0.
[4] Y. Nie, L. Li, Z. Wei, Recent advancements in Pt and Pt-free catalysts for oxygen reduction reaction, Chem. Soc. Rev. 44 (2015) 2168–2201, https://doi.org/10.1039/c4cs00484a.
[5] B.C.H. Steele, A. Heinzel, Materials for fuel-cell technologies, Nature 414 (2001) 345–352.
[6] L. Chong, G.A. Goenaga, K. Williams, H.M. Barkholtz, L.R. Grabstanowicz, J.A. Brooksbank, A.B. Papandrew, R. Elzein, R. Schlaf, T.A. Zawodzinski, J. Zou, S. Ma, D.J. Liu, Investigation of oxygen reduction activity of catalysts derived from Co and Co/Zn methyl-imidazolate frameworks in proton exchange membrane fuel cells, ChemElectroChem. 3 (2016) 1541–1545, https://doi.org/10.1002/celc.201600163.
[7] E. Proietti, F. Jaouen, M. Lefèvre, N. Larouche, J. Tian, J. Herranz, J.P. Dodelet, Iron-based cathode catalyst with enhanced power density in polymer electrolyte membrane fuel cells, Nat. Commun. 2 (2011), https://doi.org/10.1038/ncomms1427.
[8] T. Palaniselvam, B.P. Biswal, R. Banerjee, S. Kurungot, Zeolitic imidazolate framework (ZIF)-derived, hollow-core, nitrogen-doped carbon nanostructures for oxygen-reduction reactions in PEFCs, Chem. A Eur. J. 19 (2013) 9335–9342, https://doi.org/10.1002/chem.201300145.
[9] X. Lepró, E. Terrés, Y. Vega-cantú, F.J. Rodríguez-macías, H. Muramatsu, Y. Ahm, T. Hayahsi, M. Endo, Efficient anchorage of Pt clusters on N-doped carbon nanotubes and their catalytic activity Efficient anchorage of Pt clusters on N-doped carbon nanotubes and their catalytic activity, Chem. Phys. Lett. 463 (2008) 124–129, https://doi.org/10.1016/j.cplett.2008.08.001.
[10] Y. Chen, J. Wang, H. Liu, R. Li, X. Sun, S. Ye, S. Knights, Electrochemistry Communications Enhanced stability of Pt electrocatalysts by nitrogen doping in CNTs for PEM fuel cells, Electrochem. commun. 11 (2009) 2071–2076, https://doi.org/10.1016/j.elecom.2009.09.008.
[11] E. Environ, A. Morozan, B. Jousselme, S. Palacin, Low-platinum and platinum-free catalysts for the oxygen reduction reaction at fuel cell cathodes, Energy Environ. Sci. (2011) 1238–1254, https://doi.org/10.1039/c0ee00601g.
[12] K. Shen, X. Chen, J. Chen, Y. Li, Development of MOF-derived carbon-based nanomaterials for efficient catalysis, ACS Catal. 6 (2016) 5887–5903, https://doi.org/10.1021/acscatal.6b01222.
[13] H. Wang, Q.L. Zhu, R. Zou, Q. Xu, Metal-organic frameworks for energy applications, Chem 2 (2017) 52–80, https://doi.org/10.1016/j.chempr.2016.12.002.
[14] Z. Song, N. Cheng, A. Lushington, X. Sun, Recent Progress on MOF-derived nanomaterials as advanced electrocatalysts in fuel cells, Catalysts 6 (2016) 116, https://doi.org/10.3390/catal6080116.

[15] A. Zitolo, N. Ranjbar-sahraie, T. Mineva, J. Li, Q. Jia, S. Stamatin, G.F. Harrington, S.M. Lyth, P. Krtil, S. Mukerjee, E. Fonda, F. Jaouen, Identification of catalytic sites in cobalt-nitrogen-carbon materials for the oxygen reduction reaction, Nat. Commun. (2017) 1–10, https://doi.org/10.1038/s41467-017-01100-7.
[16] L. Yang, X. Zeng, W. Wang, D. Cao, Recent progress in MOF-derived, heteroatom-doped porous carbons as highly efficient electrocatalysts for oxygen reduction reaction in fuel cells, Adv. Funct. Mater. 28 (2018) 1–21, https://doi.org/10.1002/adfm.201704537.
[17] X. Shi, N. Iqbal, S.S. Kunwar, G. Wahab, H.A. Kasat, A.M. Kannan, Pt–Co@NCNTs cathode catalyst using ZIF-67 for proton exchange membrane fuel cell, Int. J. Hydrogen Energy 43 (2018) 3520–3526, https://doi.org/10.1016/j.ijhydene.2017.06.084.
[18] J. Liu, M. Jiao, L. Lu, H.M. Barkholtz, Y. Li, L. Jiang, Z. Wu, D.J. Liu, L. Zhuang, C. Ma, J. Zeng, B. Zhang, D. Su, P. Song, W. Xing, W. Xu, Y. Wang, Z. Jiang, G. Sun, High performance platinum single atom electrocatalyst for oxygen reduction reaction, Nat. Commun. 8 (2017) 1–9, https://doi.org/10.1038/ncomms15938.
[19] P.J. Ferreira, Y. Shao-Horn, D. Morgan, E.F. Holby, W.C. Sheng, S. Chen, Instability of supported platinum nanoparticles in low-temperature fuel cells, Top. Catal. 46 (2007) 285–305, https://doi.org/10.1007/s11244-007-9000-0.
[20] P. Chandran, A. Ghosh, S. Ramaprabhu, High-performance platinum-free oxygen reduction reaction and hydrogen oxidation reaction catalyst in polymer electrolyte membrane fuel cell, Sci. Rep. 8 (2018) 3591, https://doi.org/10.1038/s41598-018-22001-9.
[21] Y. Zhou, R. Pasquarelli, T. Holme, J. Berry, D. Ginley, R. O'Hayre, Improving PEM fuel cell catalyst activity and durability using nitrogen-doped carbon supports: observations from model Pt/HOPG systems, J. Mater. Chem. 19 (2009) 7830, https://doi.org/10.1039/b910924b.
[22] V.R. Stamenkovic, B. Fowler, B.S. Mun, G. Wang, P.N. Ross, C.A. Lucas, N.M. Marković, Improved oxygen reduction activity on $Pt_3Ni(111)$ via increased surface site availability, Science 315 (2007) 493–497.
[23] J. Liu, Y. Li, Z. Wu, M. Ruan, P. Song, L. Jiang, Y. Wang, G. Sun, W. Xu, Pt0.61Ni/C for high-efficiency cathode of fuel cells with superhigh platinum utilization, J. Phys. Chem. C. 122 (2018) 14691–14697, https://doi.org/10.1021/acs.jpcc.8b03966.
[24] L. Dubau, T. Asset, R. Chattot, C. Bonnaud, V. Vanpeene, J. Nelayah, F. Maillard, Tuning the performance and the stability of porous hollow PtNi/C nanostructures for the oxygen reduction reaction, ACS Catal. 5 (2015) 5333–5341, https://doi.org/10.1021/acscatal.5b01248.
[25] J. Choi, J.H. Jang, C.W. Roh, S. Yang, J. Kim, J. Lim, S.J. Yoo, H. Lee, Gram-scale synthesis of highly active and durable octahedral PtNi nanoparticle catalysts for proton exchange membrane fuel cell, Appl. Catal. B Environ. 225 (2018) 530–537, https://doi.org/10.1016/j.apcatb.2017.12.016.
[26] E. Antolini, The oxygen reduction on Pt-Ni and Pt-Ni-M catalysts for low-temperature acidic fuel cells: a review, Int. J. Energy Res. (2018) 1–23, https://doi.org/10.1002/er.4134.
[27] L. Chong, L. Chong, J. Wen, J. Kubal, F.G. Sen, J. Zou, J. Greeley, M. Chan, H. Barkholtz, W. Ding, D. Liu, Ultralow-loading platinum-cobalt fuel cell catalysts derived from imidazolate frameworks, Science 0630 (2018) 1–11.
[28] B.Y. Xia, Y. Yan, N. Li, H. Bin Wu, X.W.D. Lou, X. Wang, A metal-organic framework-derived bifunctional oxygen electrocatalyst, Nat. Energy. 1 (2016), https://doi.org/10.1038/nenergy.2015.6.
[29] J.F. Lin, X. Liu, A. Adame, R. Villacorta, J. Wertz, R. Ahmad, M. Thommes, A.M. Kannan, Development of gas diffusion layer using water based carbon slurry for proton exchange membrane fuel cells, Electrochim. Acta 56 (2011) 1591–1596, https://doi.org/10.1016/j.electacta.2010.10.019.
[30] M. Hu, J. Reboul, S. Furukawa, N.L. Torad, Q. Ji, P. Srinivasu, K. Ariga, S. Kitagawa, Y. Yamauchi, Direct carbonization of Al-based porous coordination polymer for synthesis of nanoporous carbon, J. Am. Chem. Soc. 134 (2012) 2864–2867, https://doi.org/10.1021/ja208940u.
[31] J.K. Sun, Q. Xu, Functional materials derived from open framework templates/precursors: synthesis and applications, Energy Environ. Sci. 7 (2014) 2071–2100, https://doi.org/10.1039/c4ee00517a.
[32] J. Keun, H. Jung, J. Lee, S. Yong, J. Jin, W. Seok, Metal-free CNTs grown on glass substrate by microwave PECVD, Curr. Appl. Phys. 10 (2010) 447–450, https://doi.org/10.1016/j.cap.2010.02.022.
[33] M. Shao, A. Peles, K. Shoemaker, Electrocatalysis on platinum nanoparticles : particle size effect on oxygen reduction reaction activity, Nano Lett. (2011) 3714–3719, https://doi.org/10.1021/nl2017459.
[34] J. Liu, Catalysis by supported single metal atoms, ACS Catal. 7 (2017) 34–59, https://doi.org/10.1021/acscatal.6b01534.
[35] C. Su, H. Cheng, W. Li, Z. Liu, N. Li, Z. Hou, Atomic modulation of FeCo – nitrogen – carbon bifunctional oxygen electrodes for rechargeable and flexible all-solid-state zinc – air battery, Adv. Energy Mater. 201602420 (2017) 1–12, https://doi.org/10.1002/aenm.201602420.
[36] A. Shchukarev, D. Korolkov, XPS study of group IA carbonates, Open Chem. 2 (2004) 347–362, https://doi.org/10.2478/BF02475578.
[37] R. Pietrzak, XPS study and physico-chemical properties of nitrogen-enriched microporous activated carbon from high volatile bituminous coal, Fuel 88 (2009) 1871–1877, https://doi.org/10.1016/j.fuel.2009.04.017.
[38] E. Luo, M. Xiao, J. Ge, C. Liu, W. Xing, Selectively doping pyridinic and pyrrolic nitrogen into a 3D porous carbon matrix through template-induced edge engineering: enhanced catalytic activity towards the oxygen reduction reaction, J. Mater. Chem. A (2017) 21709–21714, https://doi.org/10.1039/c7ta07608h.
[39] J. Liu, P. Song, W. Xu, Structure-activity relationship of doped-nitrogen (N)-based metal-free active sites on carbon for oxygen reduction reaction, Carbon 115 (2017) 763–772, https://doi.org/10.1016/j.carbon.2017.01.080.
[40] A. Ejaz, S. Jeon, The individual role of pyrrolic, pyridinic and graphitic nitrogen in the growth kinetics of Pd NPs on N-rGO followed by a comprehensive study on, Int. J. Hydrogen Energy 43 (2018) 5690–5702, https://doi.org/10.1016/j.ijhydene.2017.12.184.
[41] V.A. Online, 1 Introduction, (2013), pp. 5109–5118, https://doi.org/10.1039/c3nr00585b.
[42] W.S. Jung, B.N. Popov, Effect of pretreatment on durability of fct-structured pt-based alloy catalyst for the oxygen reduction reaction under operating conditions in polymer electrolyte membrane fuel cells, ACS Sustain. Chem. Eng. 5 (2017) 9809–9817, https://doi.org/10.1021/acssuschemeng.7b01728.
[43] J. Zeng, J.Y. Lee, Effects of preparation conditions on performance of carbon-supported nanosize Pt-Co catalysts for methanol electro-oxidation under acidic conditions, J. Power Sources 140 (2005) 268–273.
[44] J. Xu, X. Liu, Y. Chen, Y. Zhou, T. Lu, Y. Tang, Platinum–cobalt alloy networks for methanol oxidation electrocatalysis, J. Mater. Chem. 22 (2012) 23659–23667.
[45] P. Mani, R. Srivastava, P. Strasser, Dealloyed binary PtM3 (M = Cu, Co, Ni) and ternary PtNi 3M (M = Cu, Co, Fe, Cr) electrocatalysts for the oxygen reduction reaction: performance in polymer electrolyte membrane fuel cells, J. Power Sources 196 (2011) 666–673, https://doi.org/10.1016/j.jpowsour.2010.07.047.
[46] X.X. Wang, D.A. Cullen, Y. Pan, S. Hwang, M. Wang, Z. Feng, J. Wang, M.H. Engelhard, H. Zhang, Y. He, Y. Shao, D. Su, K.L. More, J.S. Spendelow, G. Wu, Nitrogen-coordinated single cobalt atom catalysts for oxygen reduction in proton exchange membrane fuel cells, Adv. Mater. 1706758 (2018) 1–11, https://doi.org/10.1002/adma.201706758.
[47] C.C.L. McCrory, S. Jung, J.C. Peters, T.F. Jaramillo, Benchmarking heterogeneous electrocatalysts for the oxygen evolution reaction, J. Am. Chem. Soc. 135 (2013) 16977–16987, https://doi.org/10.1021/ja407115p.
[48] L. Lin, Q. Zhu, A.W. Xu, Noble-metal-free Fe-N/C catalyst for highly efficient oxygen reduction reaction under both alkaline and acidic conditions, J. Am. Chem. Soc. 136 (2014) 11027–11033, https://doi.org/10.1021/ja504696r.